# Open-system nanocasting synthesis of nanoscale α-Fe₂O₃ porous structure with enhanced acetone-sensing properties

Xiaohong Sun [a,*], Huiming Ji [a], Xiaolei Li [a], Shu Cai [a], Chunming Zheng [b,*]

[a] School of Materials Science and Engineering, Key Lab of Advanced Ceramics and Machining Technology, Tianjin University, Tianjin 300072, PR China
[b] State Key Laboratory of Hollow-fiber Membrane Materials and Membrane Processes, School of Environmental and Chemical Engineering, Tianjin Polytechnic University, Tianjin 300387, PR China

## ABSTRACT

Nanoscale α-Fe₂O₃ with porous structure was synthesized via an open-system nanocasting method. Characterization of the crystal structures, morphologies, surface areas, and pore size distributions of the as-synthesized α-Fe₂O₃ by wide-angle and small-angle X-ray powder diffraction, scanning electron microscopy, transmission electron microscopy, and nitrogen physisorption analysis demonstrated that the nanoscale α-Fe₂O₃ synthesized in open system had a less crystallinity with average diameter of ∼6.0 nm, higher BET specific surface area of 205.4 m² g⁻¹, and wider pore size distribution from ∼2.2 nm to 15.7 nm compared with that of the mesoporous α-Fe₂O₃ synthesized in closed system. The gas-sensing measurement results revealed that the nanoscale α-Fe₂O₃ based gas sensor had a much better response to acetone than that of the device prepared from the mesoporous α-Fe₂O₃. A possible gas-sensing mechanism based on the α-Fe₂O₃ samples synthesized with different nanocasting systems was discussed in detail. Wide porous distribution of the nanoscale α-Fe₂O₃, as well as small particle size and high surface area are effective for gas molecules diffusion and formation of sufficient electron depletion area and result the enhanced sensor response, which suggests that it has great potential for practical applications in diabetes diagnosis.

© 2014 Elsevier B.V. All rights reserved.

## 1. Introduction

With the development of materials science, porous-structured metal oxide materials open a new horizon for the investigation of their advanced applications, including catalysis, energy storage, therapeutics, solar cells and sensors, etc. [1–6]. They are widely considered as good candidates for gas sensors because of their low density, high surface area and large surface–to–volume ratio than solid samples [6–8]. The interconnected pores in the porous metal oxide materials are of benefit for gas diffusion and carriers transport and have been proved to offer more active sites for chemical reaction in sensors. To date, many types of porous metal oxides have been successfully fabricated by a variety of methods, such as soft-template method via a sol–gel process [9,10] and non-template synthetic ways [11–13]. However, the above methods have been limited due to the poor porous stability during the framework formation, which leads to the loss of porous definition after high-temperature treatment. Nanocasting (hard-template method) has been proved as an efficient approach for synthesis of highly ordered porous metal oxides because of the stable support function of hard templates for high-temperature crystallization [14,15]. By now, a large number of porous metal oxides, including macroporous and mesoporous structures (Fe₂O₃, Cr₂O₃, In₂O₃, CeO₂, Co₃O₄, NiO, MoO₂ and Mn₃O₄, etc.) have been successfully prepared by using the nanocasting method [16–18].

Meanwhile, it is well recognized that the physical and chemical properties (i.e., optical, electronic, magnetic, catalytic and sensing properties, etc.) of a material strongly depend on not only its porous structure but also its particle size [19,20]. Nanoscale metal oxides have also been a hot topic in materials science and engineering because of their superior function stemming from their nanoscale dimensions and corresponding "quantum size effect" [21]. The metal oxide materials with nanoscale and porous structure as gas sensors are supposed to not only provide a large number of channels for gas diffusion, but also possess significantly large surface areas for gas-sensing reactions. However, except for the research made on the porous morphology of metal oxide gas-sensing materials, the particle size effect at the same time are seldom studied, especially in nanoscale range, since the controllable synthesis of porous metal oxide materials with varied particle size is comparably hard.

Recently, we reported an effective and universal "container effect" nanocasting method for controllable synthesis of mesoporous metal oxides ($Fe_2O_3$, $Cr_2O_3$, $In_2O_3$, $CeO_2$, $Co_3O_4$, NiO and $Mn_3O_4$) with particle size from nanometers to micrometers [22]. This provides an effective way to research the effect mechanism of particle size as well as porous structure of metal oxides on their corresponding application property.

Hematite ($\alpha$-$Fe_2O_3$), as an n-type semiconductor with a bandgap of 2.1 eV, is one of the stable semiconductor oxides under ambient conditions and has been widely applied in catalyst, gas sensor, solar energy conversion, electrode material for lithium ion batteries, and water splitting because of its good stability, low cost, excellent environmental compatibility, and easy availability [23–25]. By tuning the structure and composition of $\alpha$-$Fe_2O_3$ as a gas-sensing material, it can detect both reducing (such as ethanol, acetone, formaldehyde, CO, $NH_3$, $CH_4$, and $H_2$) and oxidizing gases (such as $Cl_2$, $O_2$ and $NO_x$) [26,27]. However, $\alpha$-$Fe_2O_3$ usually suffers from several shortcomings, such as limited maximum sensitivity, high working temperature, long response time and poor selectivity [28,29]. Porous $\alpha$-$Fe_2O_3$ and $\alpha$-$Fe_2O_3$ with nanoscale dimension are respectively reported to enhance its gas-sensing performance. For example, Mao et al. reported the enhanced formaldehyde-sensing properties of mesoporous $\alpha$-$Fe_2O_3$ with controlled porous structure [30]. Zhang et al. reported the synthesis of $\alpha$-$Fe_2O_3$ nanostructures with hierarchical flowerlike morphology and improved ethanol response [31]. Acetone is an important breath biomarker for noninvasive diagnosis of human diabetes [32]. Resistive type metal oxide acetone sensors, such as $WO_3$ and $Fe_2O_3$, exhibit significant application on the field of biomedicine and personal safety, because of their real-time detection and easy miniaturization [23,28,33]. However, fabrication of nanoscale and porous $\alpha$-$Fe_2O_3$ acetone sensor with fast response time, low detection limit and high sensitivity is still a major challenge.

In this work, we synthesized the nanoscale $\alpha$-$Fe_2O_3$ with porous structure by utilizing our previous reported "container effect" nanocasting method and compared its acetone-sensing properties with the large-sized mesoporous $\alpha$-$Fe_2O_3$. It was found that the nanoscale $\alpha$-$Fe_2O_3$ gas sensor showed a high sensitivity, fast response, and low detection limit to acetone at 240 °C. The enhanced gas-sensing mechanism was investigated in detail and was also proposed based on its porous and nanoscale structure and morphology.

## 2. Experimental

### 2.1. Preparation of ordered mesoporous silica KIT-6

All the chemical reagents are of analytical grade and are used without further purification. The mesoporous silica template KIT-6 with $Ia3d$ symmetry was prepared according to the procedure described by Ryoo and coworkers [34]. Typically, 6 g of P-123 block copolymer was dissolved in a mixture of 217 mL of deionized water and 10 mL of hydrochloric acid (36%) at 35 °C. Then 6 g of n-butanol was added and stirred for 2 h. After addition of 14 mL of tetraethylorthosilicate (TEOS, 98%), the mixture was stirred at 35 °C for another 24 h. The resulting gel was transferred to a Teflon-lined autoclave and kept for 24 h at 110 °C. The obtained sample was filtered off, washed with deionized water and dried at 60 °C. Finally, the removal of P-123 block copolymer was accomplished by calcination of the sample at 550 °C for 6 h under air atmosphere (heating rate of 2 °C min$^{-1}$).

### 2.2. "Container effect" nanocasting synthesis of nanoscale $\alpha$-$Fe_2O_3$ and mesoporous $\alpha$-$Fe_2O_3$

Nanocasting synthesis of $\alpha$-$Fe_2O_3$ using KIT-6 as hard template was previously reported by Tian and Jiao et al. [17,35]. The structure control of $\alpha$-$Fe_2O_3$ with nanoscale or mesoporous morphology was carried out by our previous improved "container effect" nanocasting method [22].

Typically, the KIT-6 silica template (1 g) was mixed with toluene (40 mL) and heated to 65 °C. Then ferric nitrate nonahydrate ($Fe(NO_3)_3\cdot 9H_2O$, 2 g) was added into the mixture under vigorous stirring. The ferric nitrate nonahydrate was melted and liquefied, and automatically moved into the template pores because of the

capillary condensation effect due to the strong interaction between nitrate and silica inner pore surface. The obtained precursor@silica composites by filtration were dried at room temperature in air overnight. Then the precursor@silica composites were calcined in a muffle furnace (Chamber Dimensions (Width × Height × Depth): 11.2 × 15.9 × 11.2 cm) with a heating rate of 2 °C min$^{-1}$ from room temperature to 400 °C and kept at that temperature for 3 h to convert the ferric nitrate precursors to $\alpha$-$Fe_2O_3$. The furnace has a smog tube with diameter of 1.6 mm on its top. During calcination, different container effect (open system or closed system) were used for the synthesis of $\alpha$-$Fe_2O_3$ with different morphologies but the calcination temperature program was kept the same. For the synthesis of nanoscale $\alpha$-$Fe_2O_3$, the Petri dish (open system) with diameter of 50 mm and depth of 10 mm was used as the thermal-treatment container (see Fig. 1a). For the synthesis of mesoporous $\alpha$-$Fe_2O_3$, the glass bottle (diameter of 16 mm and depth of 51 mm) as thermal-treatment container was covered with a glass strip with 100% coverage (closed system, see Fig. 1b). Such differences in the container conditions during calcination are sufficient to change the atomic ordering and morphology of the $\alpha$-$Fe_2O_3$ and have a profound influence on their gas-sensing behavior, as demonstrated later. After calcination, the resulting $\alpha$-$Fe_2O_3$@silica samples were treated with 2 M NaOH solution twice to remove the silica template. Final products were recovered by centrifuging and washing with water and ethanol for several times.

### 2.3. Characterization

The wide-angle X-ray powder diffraction (XRD) patterns of the dry samples were performed at room temperature on a Rigaku D/max 2500 diffractometer with a graphite monochromator and Cu K$\alpha$ radiation ($\lambda = 0.154$ nm). Typically, the data were collected from 20° to 70° with a resolution of 0.2°. The average crystallite size was estimated from the Debye–Scherrer equation, $D = K\lambda/(\beta \cos \theta)$, where $D$ is the average crystal diameter, $\beta$ is the corrected peak width (full width at half-maximum), $K$ is a constant related the shape of the crystallites ($K = 0.94$), $\lambda$ is the wavelength of the X-rays employed, and $\theta$ is the diffraction angle. The width of the diffraction peak with the highest intensity was selected for the calculation. The small-angle X-ray diffraction (SAXRD) data were taken on a Philips X'pert MPD thin film powder XRD using an Cu K$\alpha$ radiation ($\lambda = 0.154$ nm). Scanning Electron Microscopy (SEM) was measured on a FEI XL40 instrument. Transmission Electron Microscopy (TEM) was performed on a Philips Tecnai F20 microscope, 200 kV, equipped with a field emission gun. All samples subjected to TEM measurement were ultrasonically dispersed in alcohol and drop-cast onto a copper grid coated with an amorphous carbon film and then dried in air. Nitrogen adsorption and desorption isotherms were measured at 77 K on a Micromeritics TriStar porosimiter apparatus. The samples were outgassed at 150 °C overnight before measurements were made. The surface area was obtained by the Brunauer–Emmett–Teller (BET) method and the pore size distribution was calculated from the adsorption branch of the isotherm using the Barrett–Joyner–Halanda (BJH) method.

### 2.4. Gas sensor fabrication and measurement

The gas sensors were fabricated by dip-coating a water paste of $\alpha$-$Fe_2O_3$ onto alumina ceramic tube with gold electrodes (shown in Fig. 1c). The paste was prepared by mixing of 0.5 mL of deionized water and 50 mg of $\alpha$-$Fe_2O_3$. In order to control the operating temperature, a Ni–Cr heating wire was inserted into the tube to form an indirect-heated gas sensor. Electrical contacts were made with two platinum wires attached to each gold electrode. The as-modified electrode was dried under infrared lamp before use. The gas-sensing properties of $\alpha$-$Fe_2O_3$ were measured by a CGS-8 series gas-sensing measurement system under a steady-state condition in an organic glass chamber with a volume of 20 L (Beijing Elite Tech Co., Ltd., China). The relative humidity (RH) was about 40%. An appropriate amount of gas vapor was injected into the closed chamber by a microinjector, and the sensor was exposed to air again by opening the chamber when the test was completed. The response (sensitivity, $S = R_a/R_g$) of the sensor was defined as the ratio of sensor resistance in dry air ($R_a$) to that in a target gas ($R_g$). The response and recovery times were defined as the times required for a change in the resistance to reach 90% of the
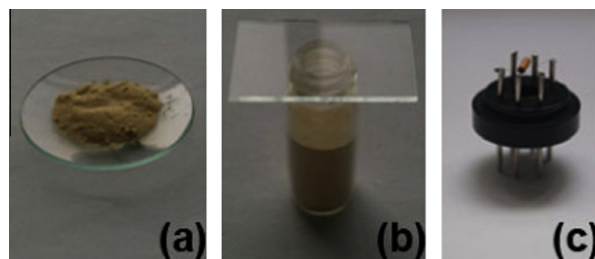


**Fig. 1.** Thermal-treatment container of nanoscale $\alpha$-$Fe_2O_3$ (a) and mesoporous $\alpha$-$Fe_2O_3$ (b); scheme of $\alpha$-$Fe_2O_3$ gas sensor.

equilibrium value after the detected gas was injected and removed, respectively. Acetone, ethanol, methanol, toluene and formaldehyde were used as the detecting gas.

## 3. Results and discussion

### 3.1. Nanocasting synthesis of α-Fe₂O₃ by "container effect"

In our previous work, "container effect" nanocasting method was found to be an effective and versatile way to synthesize ordered mesoporous metal oxides with continuous controlled porous regularity and particle sizes by adjusting the calcination container opening accessibility or shapes and sizes [22]. It can be ascribed to the influence of the container on the escape rate of water and nitrogen oxide byproducts, which in turn affects the conversion mechanism of metal precursors and the structure of final metal oxide products (from highly ordered mesoporous structure to nano-particles assembly). In closed system, the "liquid–to–solid" conversion occurs for the metal precursors to metal oxide. The quasi-sealed container prevents the fast evaporation of water vapor and nitrogen oxide byproducts and keeps the metal precursor in an aqueous liquid form until it reaches the decomposition temperature of metal precursor. Then metal oxide crystal seeds are precipitate directly from the liquid precursor solution, which facilitates the formation of large particles, since metal species can easily transport inside the mesopore channels in a solution form. In contrast, when an open Petri dish is used as container (open system), escaping water and byproduct are rapidly evaporated up to the open space after metal precursor is melted, which causes solidification of the precursors before their decomposition. The "solid–to–solid" conversion inhibits the long-distance transportation of the metal species and thus only isolated nanoparticles are formed inside the mesopore channels. "Container effect" nanocasting method supplied a solution to research the relationship between the applied performance of metal oxides and their porous morphology, as well as particle sizes and crystallinity. In this work, α-Fe₂O₃ was selected as the model material to research the function of "container effect" nanocasting method to their gas-sensing performance. Open system (Petri dish as container) and closed system (glass bottle with 100% coverage as container) were used to carry out the container effect with two extremes and change the morphology and structure of α-Fe₂O₃ with different particle size, porous distribution and crystallinity.

Fig. 2a shows the XRD patterns of the nanocasting synthesized Fe₂O₃ by the "container effect". All the peaks of mesoporous Fe₂O₃ synthesized by thermal treatment in closed system can be readily indexed as pure rhombohedral phase of Fe₂O₃, α-Fe₂O₃, which is in good agreement with the values from the standard card (JCPDS No. 33-0664). No characteristic peaks were observed for other impurities such as ferrous oxide or magnetite. By the Debye–Scherrer equation, the average crystallite size of mesoporous α-Fe₂O₃ is calculated to be 11.6 nm. The XRD pattern of nanoscale α-Fe₂O₃ synthesized by thermal treatment in open system shows two weak and broad diffraction peaks, suggesting a smaller particle size and less crystallinity compared to that of the mesoporous α-Fe₂O₃. Fig. 2b shows the SAXRD patterns of KIT-6 template, mesoporous α-Fe₂O₃ and nanoscale α-Fe₂O₃. The peaks of KIT-6 observed at (2 1 1) and (2 2 0) reflections reveal that the template consists uniquely of large ordered mesoporous domains of pure bicontinuous mesostructure with cubic Ia3d symmetry. The SAXRD pattern of mesoporous α-Fe₂O₃ shows one intense peak at 2θ of around 0.93°, corresponding to the 211 diffraction peak of Ia3d symmetry, which indicates that the long-range mesostructured regularity of KIT-6 is well retained in mesoporous α-Fe₂O₃ replica. The disappearance of the shoulder peak at 2θ = 1.04° indicates that the mesoporous structure of mesoporous α-Fe₂O₃ is lower than that
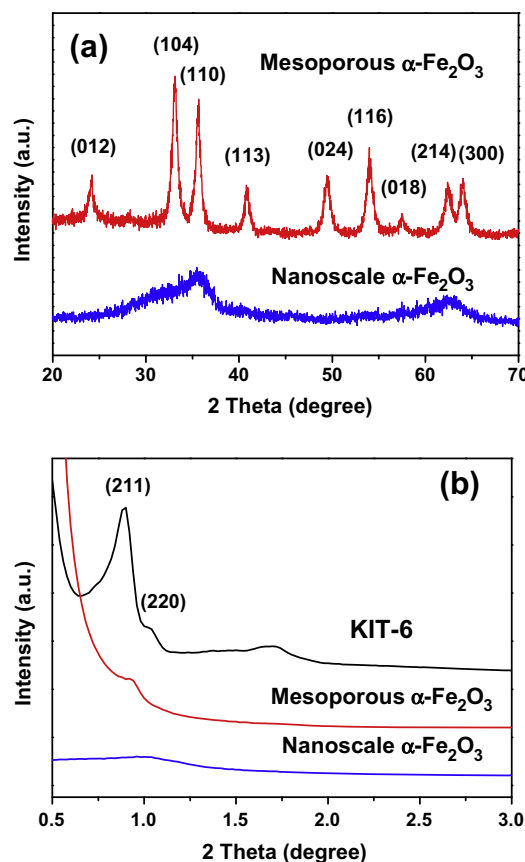


**Fig. 2.** XRD patterns (a) of nanoscale α-Fe₂O₃ and mesoporous α-Fe₂O₃; SAXRD patterns (b) of KIT-6, nanoscale α-Fe₂O₃ and mesoporous α-Fe₂O₃.

of KIT-6. Comparing to the SAXRD pattern of mesoporous α-Fe₂O₃, the intensity of the 211 diffraction peak for nanoscale α-Fe₂O₃ obviously decreases, which can be interpreted as a reduction in the X-ray scattering contrast between the pore and the framework [36], revealing that the mesostructured ordering of nanoscale α-Fe₂O₃ is lower than that of mesoporous α-Fe₂O₃.

SEM and TEM analysis provided further insight into the porous morphology and particle size of the as-obtained products. Fig. 3a–d shows the SEM and TEM images of the α-Fe₂O₃ synthesized by thermal treatment in different container conditions. It can be clearly observed that α-Fe₂O₃ synthesized in open system (Fig. 3a and c) are composed of a large number of isolated and small nanoparticles with grain size of ~6.0 nm without long-range mesoporous periodicity, which agrees with the SAXRD result [22]. Meanwhile, among the interconnected nanoparticles a large amount of voids with wide distribution exit and result in highly porous property of the nanoscale α-Fe₂O₃. The nanoscale morphology and porous structure arise from the "solid–to–solid conversion" mechanism for "container effect" nanocasting synthesis [22]. From the SEM and TEM images of α-Fe₂O₃ synthesized in closed system (Fig. 3b and d), one can see that the product particles are nearly-ellipse shape and highly ordered with periodic cubic (Ia3d) mesostructure. The particle size is ~200 nm with porous wall thickness of ~6.6 nm and porous size of ~2.6 nm. The long mesoporous periodicity and large particle size arise from the "liquid–to–solid conversion" mechanism for "container effect" nanocasting synthesis [22,37].

### 3.2. Gas-sensing performance

It is well known that the optimal operating temperature of a gas sensor for detecting a given gas is an important issue, which is
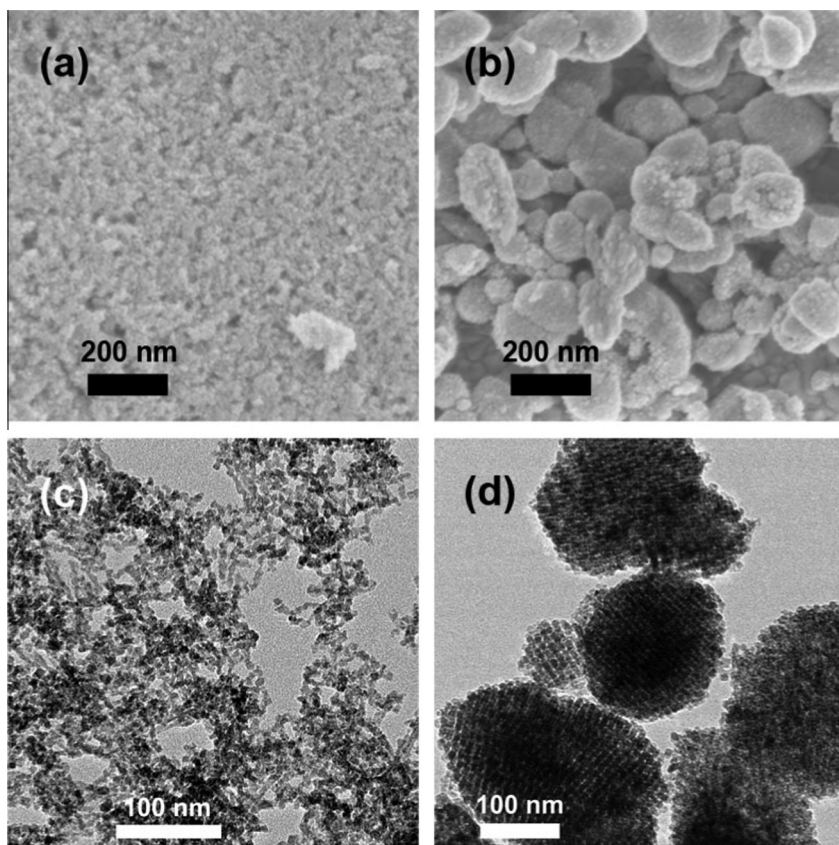
**Fig. 3.** SEM images of nanoscale α-Fe₂O₃ (a) and mesoporous α-Fe₂O₃ (b); TEM images of nanoscale α-Fe₂O₃ (c) and mesoporous α-Fe₂O₃ (d).

obtained by performing the gas-sensing response at different operating temperatures. Fig. 4a displays the sensitivity of the as-synthesized α-Fe₂O₃ sensors toward 100 ppm of acetone as a function of the operating temperature. One can see that the response of the nanoscale α-Fe₂O₃ sensor presents a rapid increase and reaches its maximum value of 15.7 at 240 °C, then gradually decreases with further increasing of the operating temperature. The mesoporous α-Fe₂O₃ sensor displays the similar response tendency and its sensitivity reaches the maximum value of 7.0 at the same operating temperature of 240 °C. This phenomenon is commonly observed for many semiconducting metal oxide based sensors and can be explained by the balance between the speed of chemical reaction and the speed of gas diffusion [38,39]. At low temperatures, the response gradually rises with the increasing of operating temperature. Nevertheless, the diffusion speed of the target gas is also accelerated at high temperature. Thus, the above two processes will tend to balance at a certain temperature, at which the sensitivity of the sensors reaches the maximum [40,41]. From the above results, the nanoscale α-Fe₂O₃ sensor shows the enhanced sensitivity and 240 °C is the optimum operating temperature for α-Fe₂O₃ gas sensors and is used in the following gas-sensing test.

Rapid response and recovery characteristics are required for gas sensor, which are defined as the time to reach 90% of the final equilibrium value after the detected gas is injected and removed, respectively [42]. Fig. 4b and c shows the typical dynamic gas-sensing curves of the nanoscale α-Fe₂O₃ and mesoporous α-Fe₂O₃, respectively to 100 ppm of acetone. The resistance drops abruptly once the acetone is injected, stays stable at a low value and then increases back immediately after the acetone has been eliminated. The response time and recovery time of the nanoscale α-Fe₂O₃ sensor is 0.8 s and 27.0 s, respectively, which is obviously faster than that of the mesoporous α-Fe₂O₃ sensor (with response

time and recovery time of 1.7 s and 76.0 s, respectively). This indicates that the nanoscale α-Fe₂O₃ synthesized by the open-system nanocasting method causes a clear enhancement in gas sensitivity.

It is known that the development of gas sensor which can sense gas at lower detection concentration and allow quantification of gas over a wide concentration range is of practical interest. Fig. 5a and b shows the representative dynamic responses as a function of acetone concentration for the α-Fe₂O₃ sensors synthesized in different container conditions. It is obvious that both α-Fe₂O₃ based sensors have a wide detection range for acetone from 500 ppb to 100 ppm. With the increasing of acetone concentration, the responses greatly increase. The sensitivities of both α-Fe₂O₃ sensors as a function of acetone concentration are provided in Fig. 5c. It can be seen that the nanoscale α-Fe₂O₃ sensor is more sensitive than the mesoporous α-Fe₂O₃ sensor. Taking 50 ppm as an example, the nanoscale α-Fe₂O₃ sensor exhibits a sensitivity of 10.5, which is more than twice higher than that (4.7) of the mesoporous α-Fe₂O₃ sensor. The sensitivity value to the lowest acetone detection limit of 500 ppb for nanoscale α-Fe₂O₃ sensor is ∼ 1.5, whereas that of the mesoporous α-Fe₂O₃ sensor is ∼ 1.2. In short, the nanoscale α-Fe₂O₃ sensor shows an enhanced response to acetone compared to the mesoporous α-Fe₂O₃ even at the lowest detection limit. It should also be pointed out that the nanoscale α-Fe₂O₃ sensor also possesses better performance when compared with some of the other nanostructured α-Fe₂O₃ acetone sensors reported in previous work [24,31], which means that the open-system nanocasting method is an effective way to synthesize highly sensitive α-Fe₂O₃ based acetone sensor.

Selectivity is another very important parameter for a utility-type metal oxide gas sensor, because poor selectivity will induce mistaken alarm and limit its extensive utilization. In our experiment, acetone, ethanol, methanol, toluene and formaldehyde
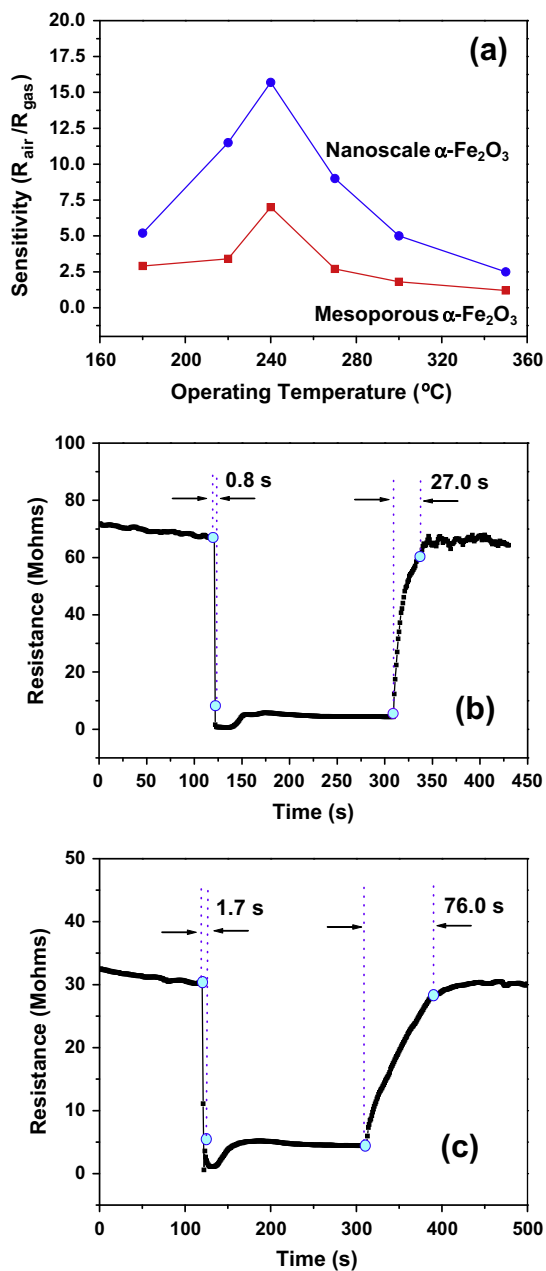
**Fig. 4.** The sensitivity versus operating temperature of nanoscale α-Fe₂O₃ and mesoporous α-Fe₂O₃ exposed to 100 ppm of acetone (a); dynamic gas sensing transient of nanoscale α-Fe₂O₃ to 100 ppm of acetone at 240 °C (b); dynamic gas sensing transient of mesoporous α-Fe₂O₃ to 100 ppm of acetone at 240 °C (c).

**Fig. 5.** Typical response and recovery curves to different acetone concentration of nanoscale α-Fe₂O₃ (a) and mesoporous α-Fe₂O₃ (b); sensor sensitivity of nanoscale α-Fe₂O₃ and mesoporous α-Fe₂O₃ with varied acetone concentration (c).

sensing characteristics of both α-Fe₂O₃ based sensors are measured at 240 °C with concentration of 100 ppm as shown in Fig. 6. According to the results, it is clear that the responses of the nanoscale α-Fe₂O₃ sensor to all test gases are significantly larger than those of the mesoporous α-Fe₂O₃ sensor, indicating that the sensing ability of the nanocasting synthesized α-Fe₂O₃ has been effectively improved by the open-system calcination method. Meanwhile, both α-Fe₂O₃ sensors prefer to respond to acetone vapor, and show less sensitivity to other gases. That is to say, the present sensors display quite excellent selectivity to acetone, especially the nanoscale α-Fe₂O₃ synthesized by the open-system nanocasting method, of which the responses reach 15.7, 10.9, 6.7, 4.9 and 2.3 to acetone, ethanol, methanol, toluene and formaldehyde, respectively.
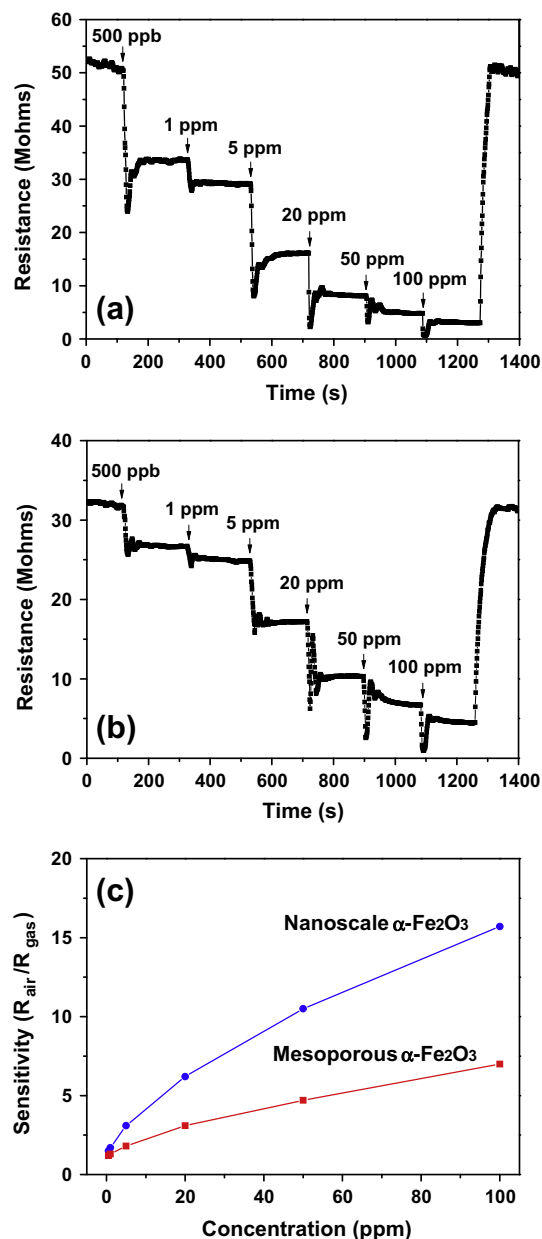
### 3.3. Mechanism research

It is known that the gas-sensing mechanism of α-Fe₂O₃ is based on surface chemisorption of gas molecules and electron donation, resulting in a decrease in the resistance of sensor [43]. α-Fe₂O₃ is an n-type semiconductor with deficiency of oxygen in the ambient environment. Once exposed to air, oxygen molecules are adsorbed on the surface and form $O_2^-$, $O^{2-}$, and $O^-$ ions through trapping the electrons from the conductance band of α-Fe₂O₃, and resulting the increase of the resistance and the formation of electron depletion layer. When exposed to test gases such as acetone, gas molecules are adsorbed and oxidized at the active sites by the adsorbed oxygen, and then release electrons to the surface of α-Fe₂O₃. Thus, the resistance of the sensor is eventually decreased.

In general, the sensing performance of metal oxides depends on several factors, such as particle size, crystal defects, surface areas,
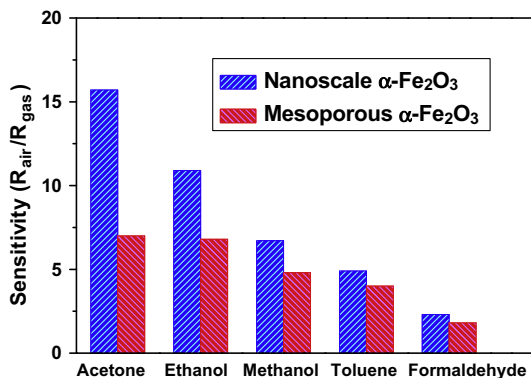
**Fig. 6.** Sensitivity values of nanoscale $\alpha$-Fe$_2$O$_3$ and mesoporous $\alpha$-Fe$_2$O$_3$ to 100 ppm of various gases: acetone, ethanol, methanol, toluene and formaldehyde.



**Fig. 7.** Nitrogen physisorption isotherms (a) and pore size distributions (b) of nanoscale $\alpha$-Fe$_2$O$_3$ and mesoporous $\alpha$-Fe$_2$O$_3$.



**Fig. 8.** Illustration of respective sensing factors of nanoscale $\alpha$-Fe$_2$O$_3$ and mesoporous $\alpha$-Fe$_2$O$_3$.

and porous structure of the nanoscale $\alpha$-Fe$_2$O$_3$ play a major role in the enhanced gas-sensing performance. The nitrogen physisorption isotherms and pore size distributions of the nanoscale $\alpha$-Fe$_2$O$_3$ and mesoporous $\alpha$-Fe$_2$O$_3$ are shown in Fig. 7. The BET specific surface area of the nanoscale $\alpha$-Fe$_2$O$_3$ (205.4 m$^2$ g$^{-1}$) is much higher than that of the mesoporous $\alpha$-Fe$_2$O$_3$ (109.1 m$^2$ g$^{-1}$), which can offer more contact sites and make the adsorption and reaction of oxygen and acetone molecules more easy. In Fig. 7a, both $\alpha$-Fe$_2$O$_3$ samples exhibit a type IV isotherm with a type H3 hysteresis loop, indicating the characteristics of the materials with mesopores [42]. The large hysteresis loop of the nanoscale $\alpha$-Fe$_2$O$_3$ involving the capillary condensation suggests the presence of a large number of interconnected mesopore networks, which confirms the observation from SEM and TEM images (Fig. 3). The BJH analysis (Fig. 7b) shows that the nanoscale $\alpha$-Fe$_2$O$_3$ exhibits a wide pore size distribution ranging from ~2.2 nm to 15.7 nm calculated from the adsorption branch of the nitrogen adsorption isotherm, whereas that for the mesoporous $\alpha$-Fe$_2$O$_3$ is from ~2.1 nm to 3.5 nm. Tiemann et al. indicated that Knudsen diffusion is the main diffusion type for metal oxide sensing materials and bigger pores are favorable for the diffusion of gas molecules [6]. The mesoporous $\alpha$-Fe$_2$O$_3$ with larger particle size and smaller ordered mesopores makes the diffusion of target gases within the sensing layer comparably hard, and results the short effective diffusion distance and small electron depletion area, which leads to the lower gas sensitivity performance, compared with that of the nanoscale $\alpha$-Fe$_2$O$_3$ (Fig. 8). On the contrary, small particle size and high surface area of the nanoscale $\alpha$-Fe$_2$O$_3$ with wide pore size distribution, including small intraparticle mesopores from nanocasting and big interparticle mesopores from particle pile, are effective for gas molecules diffusion and formation of sufficient electron depletion area and results the enhanced sensor response (Fig. 8).

## 4. Conclusions

In summary, the nanoscale $\alpha$-Fe$_2$O$_3$ porous structure has been successfully constructed via the open-system nanocasting strategy. An enhanced sensing property to acetone, including high response value, fast response characteristic and good selectivity was demonstrated in comparison to the mesoporous $\alpha$-Fe$_2$O$_3$. The small particle size, high surface area, and wide pore size distribution, including small intraparticle mesopores from nanocasting and big interparticle mesopores from particle pile are probably responsible for the enhanced gas-sensing performance. These results make nanoscale $\alpha$-Fe$_2$O$_3$ with porous structure good candidate for fabricating high performance acetone sensors in practical.

## Acknowledgments

and porous structures, which greatly affect the adsorption and diffusion of gas molecules and carriers mobility [44–46]. From the above results, we can see that the acetone-sensing performance of $\alpha$-Fe$_2$O$_3$ has been greatly improved by the open-system nanocasting synthesis. The enhanced gas-sensing properties of the nanoscale $\alpha$-Fe$_2$O$_3$ synthesized in open system can be attributed to the following factors. Firstly, the particle size of the nanoscale $\alpha$-Fe$_2$O$_3$ (~6.0 nm) is less than the reported Debye length (~44 nm) of $\alpha$-Fe$_2$O$_3$ [47], which is beneficial to the gas-sensing improvement [48]. Secondly, in comparison to the highly crystalline mesoporous $\alpha$-Fe$_2$O$_3$, the nanoscale $\alpha$-Fe$_2$O$_3$ with smaller particle size and less crystallinity have more exposed defects of low-coordinated atoms that are located on the surfaces and promote the gas reaction [43,49,50]. Moreover, the high surface area
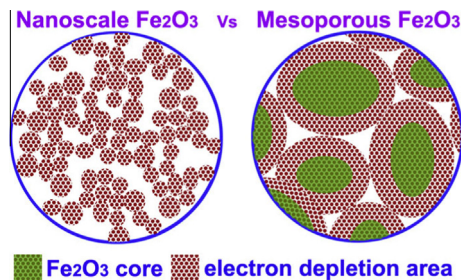
## References

[1] Y.H. Deng, J. Wei, Z.K. Sun, D.Y. Zhao, Chem. Soc. Rev. 42 (2013) 4054–4070.
[2] J.B. Wu, R.Q. Guo, X.H. Huang, Y. Lin, J. Power Sources 243 (2013) 317–322.
[3] J.C. Rooke, T. Barakat, M.F. Finol, P. Billemont, G. De Weireld, Y. Li, R. Cousin, J.M. Giraudon, S. Siffert, J.F. Lamonier, B.L. Su, Appl. Catal. B – Environ. 142 (2013) 149–160.
[4] A. Ampoumogli, T. Steriotis, P. Trikalitis, D. Giasafaki, E.G. Bardaji, M. Fichtner, G. Charalambopoulou, J. Alloys Comp. 509 (2011) S705–S708.
[5] Y. Ren, Z. Ma, P.G. Bruce, Chem. Soc. Rev. 41 (2012) 4909–4927.
[6] T. Wagner, S. Haffer, C. Weinberger, D. Klaus, M. Tiemann, Chem. Soc. Rev. 42 (2013) 4036–4053.
[7] H.J. Kim, J.H. Lee, Sensor. Actuat. B – Chem. 192 (2014) 607–627.
[8] J. Liu, Z.P. Guo, K.X. Zhu, W.J. Wang, C.F. Zhang, X.L. Chen, J. Mater. Chem. 21 (2011) 11412–11417.
[9] E.M. Masoud, J. Alloys Comp. 585 (2014) 357–361.
[10] J. Fan, S.W. Boettcher, G.D. Stucky, Chem. Mater. 18 (2006) 6391–6396.
[11] X.H. Liu, J. Zhang, X.Z. Guo, S.H. Wu, S.R. Wang, Nanotechnology 21 (2010) 095501.
[12] J. Zhang, S. Wang, M. Xu, Y. Wang, B. Zhu, S. Zhang, W. Huang, S. Wu, Cryst. Growth Des. 9 (2009) 3532–3537.
[13] H.P. Cong, S.H. Yu, Cryst. Growth Des. 9 (2009) 210–217.
[14] W. Li, D.Y. Zhao, Chem. Commun. 49 (2013) 943–946.
[15] A.H. Lu, F. Schuth, Adv. Mater. 18 (2006) 1793–1805.
[16] Y. Shi, B. Guo, S.A. Corr, Q. Shi, Y.-S. Hu, K.R. Heier, L. Chen, R. Seshadri, G.D. Stucky, Nano Lett. 9 (2009) 4215–4220.
[17] F. Jiao, A. Harrison, J.C. Jumas, A.V. Chadwick, W. Kockelmann, P.G. Bruce, J. Am. Chem. Soc. 128 (2006) 5468–5474.
[18] L.L. Li, W.T. Duan, Q. Yuan, Z.X. Li, H.H. Duan, C.H. Yan, Chem. Commun. 41 (2009) 6174–6176.
[19] S. Eickhoff, C. Zhang, T. Cui, J. Power Sources 243 (2013) 562–568.
[20] F. Amano, E. Ishinaga, A. Yamakata, J. Phys. Chem. C 117 (2013) 22584–22590.
[21] M.E. Franke, T.J. Koplin, U. Simon, Small 2 (2006) 36–50.
[22] X.H. Sun, Y.F. Shi, P. Zhang, C.M. Zheng, X.Y. Zheng, F. Zhang, Y.C. Zhang, N.J. Guan, D.Y. Zhao, G.D. Stucky, J. Am. Chem. Soc. 133 (2011) 14542–14545.
[23] X.J. Liu, Z. Chang, L. Luo, X.D. Lei, J.F. Liu, X.M. Sun, J. Mater. Chem. 22 (2012) 7232–7238.
[24] W. Yan, H.Q. Fan, Y.C. Zhai, C. Yang, P.R. Ren, L.M. Huang, Sensor. Actuat. B – Chem. 160 (2011) 1372–1379.
[25] O.M. Lemine, I. Ghiloufi, M. Bououdina, L. Khezami, M.O. Mhamed, A.T. Hassan, J. Alloys Comp. 588 (2014) 592–595.
[26] J. Zhang, X.H. Liu, L.W. Wang, T.L. Yang, X.Z. Guo, S.H. Wu, S.R. Wang, S.M. Zhang, Nanotechnology 22 (2011) 185501.
[27] X.Y. Lai, J. Li, B.A. Korgel, Z.H. Dong, Z.M. Li, F.B. Su, J.A. Du, D. Wang, Angew. Chem. – Int. Ed. 50 (2011) 2738–2741.
[28] P. Gunawan, L. Mei, J. Teo, J.M. Ma, J. Highfield, Q.H. Li, Z.Y. Zhong, Langmuir 28 (2012) 14090–14099.
[29] J. Ming, Y.Q. Wu, L.Y. Wang, Y.C. Yu, F.Y. Zhao, J. Mater. Chem. 21 (2011) 17776–17782.
[30] D. Mao, J.X. Yao, X.Y. Lai, M. Yang, J.A. Du, D. Wang, Small 7 (2011) 578–582.
[31] L.L. Wang, T. Fei, Z. Lou, T. Zhang, ACS Appl. Mater. Interface 3 (2011) 4689–4694.
[32] M. Righettoni, A. Tricoli, S.E. Pratsinis, Anal. Chem. 82 (2010) 3581–3587.
[33] L. Wang, A. Teleki, S.E. Pratsinis, P.I. Gouma, Chem. Mater. 20 (2008) 4794–4796.
[34] F. Kleitz, S.H. Choi, R. Ryoo, Chem. Commun. 17 (2003) 2136–2137.
[35] B.Z. Tian, X.Y. Liu, H.F. Yang, S.H. Xie, C.Z. Yu, B. Tu, D.Y. Zhao, Adv. Mater. 15 (2003) 1370–1374.
[36] X.Y. Lai, D. Wang, N. Han, J. Du, J. Li, C.J. Xing, Y.F. Chen, X.T. Li, Chem. Mater. 22 (2010) 3033–3042.
[37] X.H. Sun, Y.F. Shi, H.M. Ji, X.L. Li, S. Cai, C.M. Zheng, J. Alloys Comp. 545 (2012) 5–11.
[38] H. Shan, C.B. Liu, L. Liu, J.B. Zhang, H.Y. Li, Z. Liu, X.B. Zhang, X.Q. Bo, X. Chi, ACS Appl. Mater. Interface. 5 (2013) 6376–6380.
[39] Q. Qi, T. Zhang, L. Liu, X.J. Zheng, G.Y. Lu, Sensor. Actuat. B – Chem. 141 (2009) 174–178.
[40] S.K. Lim, S.H. Hwang, D. Chang, S. Kim, Sensor. Actuat. B – Chem. 149 (2010) 28–33.
[41] X.F. Chu, S.M. Liang, T.Y. Chen, Q.F. Zhang, Mater. Chem. Phys. 123 (2010) 396–400.
[42] F. Yang, H.L. Su, Y.Q. Zhu, J.J. Chen, W.M. Lau, D. Zhang, Scr. Mater. 68 (2013) 873–876.
[43] Y.L. Cao, H.Y. Luo, D.Z. Jia, Sensor. Actuat. B – Chem. 176 (2013) 618–624.
[44] J.T. Zai, J. Zhu, R.R. Qi, X.F. Qian, J. Mater. Chem. A 1 (2013) 735–745.
[45] C.H. Zhao, G.Z. Zhang, W.H. Han, J.C. Fu, Y.M. He, Z.X. Zhang, E.Q. Xie, Crystengcomm 15 (2013) 6491–6497.
[46] Y. Wang, J.L. Cao, M.G. Yu, G. Sun, X.D. Wang, H. Bala, Z.Y. Zhang, Mater. Lett. 100 (2013) 102–105.
[47] K.R.G. Karthik, H.K. Mulmudi, K.B. Jinesh, N. Mathews, C.H. Sow, Y.Z. Huang, S.G. Mhaisalkar, Appl. Phys. Lett. 99 (2011) 132105.
[48] A. Tricoli, M. Righettoni, A. Teleki, Angew. Chem. – Int. Edit. 49 (2010) 7632–7659.
[49] Y.X. Qin, F. Wang, W.J. Shen, M. Hu, J. Alloys Comp. 540 (2012) 21–26.
[50] N.D. Hoa, V.V. Quang, D. Kim, N.V. Hieu, J. Alloys Comp. 549 (2013) 260–268.